Wide-band high-efficiency optical-to-electrical conversion stimulus probe heads for testing large-signal responses of high-speed electronic devices

doi: 10.1109/22.763150

Wide-Band High-Efficiency Optical-to-Electrical Conversion Stimulus Probe Heads for Testing Large-Signal Responses of High-Speed Electronic Devices

Taiichi Otsuji, *Member, IEEE,* Kazutoshi Kato, *Member, IEEE,* Shunji Kimura, *Member, IEEE,* and Tadao Nagatsuma, *Member, IEEE*

***Abstract*— Wide-band high-efficiency optical-to-electrical conversion stimulus probe heads have been developed for testing large-signal responses of high-speed electronic devices. Two types of such probes were demonstrated using a 1.55-μm 85-GHz-bandwidth waveguide p-i-n photodiode. The type-I probe employs a simple semirigid coaxial cable with a bias network for the electrical-signal transmission, resulting in a very low modal dispersion of $<$1.0 ps. The highest $-$3-dB bandwidth of 60 GHz was obtained for an output voltage of 250 $mV_{p\text{-}p}$, and was maintained beyond 50 GHz for output voltages of up to 400 $mV_{p\text{-}p}$. The type-II probe employs a broad-band InP high electron-mobility transistor distributed amplifier that boosts the electrical output signal amplitude over 1 $V_{p\text{-}p}$. The $-$3-dB bandwidth is 40 (35) GHz for output voltages up to 500 (1000) $mV_{p\text{-}p}$.**

***Index Terms*—Amplifier, coaxial cable, optoelectronics, photodiode, probe head.**

I. Introduction

RECENT progress in semiconductor devices has brought near 100-GHz bandwidth to electronic analog and digital integrated circuits (IC's) [1], [2]. Optoelectronic techniques using picosecond or femtosecond laser pulses are the most promising methods for characterizing these ultra-broad-band electronic devices. Ultrafast time-domain electromagnetic response of these devices has been observed by means of pump-probe techniques based on electrooptic [3]–[6] or photoconductive [7]–[10] sampling. Over the past 20 years, various high-speed optoelectronic wafer-probing techniques have been developed. The fundamental optoelectronic wafer-probing setups include ultrafast optical-to-electrical (OE) converters to generate ultrashort electrical pulses to excite the device-under-test (DUT), and electrooptic materials or photoconductors to detect the electromagnetic response of DUT's. Photoconductors have been mainly used for the OE converters. Traditionally, wirebonds or beam leads are used to connect external photoconductors to the DUT or monolithically integrated photoconductors and transmission lines are used as part of the test wafer. For both cases, flexibility in probing points and reproducibility of the stimulus signal are heavily sacrificed.

Recently, a picosecond OE conversion stimulus probe head has been developed for use in pump-probe measurements [11]–[14] where photoconductors are put onto the probe tip. The photoconductive probe can be moved to contact various sites on a wafer, then drastically improved the testing flexibility and reproducibility. The sensitive bias dependence of the photoconductors are utilized as a fast voltage sensor so that both stimulus and/or detection functions can be easily performed by a single probe head [11]–[14]. This is another merit for the use of photoconductors. However, in spite of their excellent bandwidths exceeding 200 GHz, pulse-pattern injections over 10-Gb/s with $>$100-mV height have not been attained because of their low responsivities of less than 0.1 A/W and/or saturation limit, those of which are inherent properties of the photoconductors. To achieve large-signal pulse-pattern response measurements at real operating bit rates in analog and digital IC's near 100 Gb/s, highly efficient OE conversion probes with flat broad-band response as well as ultrahigh bit-rate optical pulse-pattern generators are essential [15].

To cope with large-signal injection at high data rates, the authors have reported on the first trial of an OE conversion stimulus probe head employing a waveguide p-i-n photodiode (WGPD) with a high responsivity of 0.75 A/W, an output saturation voltage of 400 $mV_{p\text{-}p}$, and a bandwidth of 50 GHz [15]–[17]. However, its current performance does not meet the requirements for measurements of high-end (beyond 40 Gbit/s) analog and digital IC's. The coplanar waveguide (CPW) that configured the transmission line degraded the waveform symmetry because of its modal frequency dispersion, which limits the effective $-$3-dB bandwidth [17]. It is also true that near 1-$V_{p\text{-}p}$ output voltage is essential for testing high-speed digital IC's.

This paper describes two types of wide-band high-efficiency OE conversion stimulus probe heads for testing large-signal responses of high-speed electronic devices. Both of them

Manuscript received March 14, 1997; revised November 25, 1998.

T. Otsuji was with the Nippon Telegraph and Telephone Corporation (NTT) Network Innovation Laboratories, Kanagawa 239-0847, Japan. He is now with the Department of Control Engineering and Science, Kyushu Institute of Technology, Fukuoka 820-8502, Japan.

K. Kato is with the Nippon Telegraph and Telephone Corporation (NTT) Photonics Laboratories, Kanagawa 243-0198, Japan.

S. Kimura is with the Nippon Telegraph and Telephone Corporation (NTT) Network Innovation Laboratories, Kanagawa 239-0847, Japan.

T. Nagatsuma is with the Nippon Telegraph and Telephone Corporation (NTT) System Telecommunications Energy Laboratories, Kanagawa 243-0198, Japan.

Publisher Item Identifier S 0018-9480(99)03120-8.

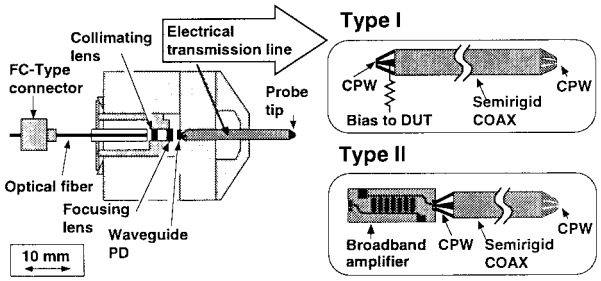

Fig. 1. Schematic of optoelectronic active stimulus probe head. The Type-II probe employs a broad-band amplifier.

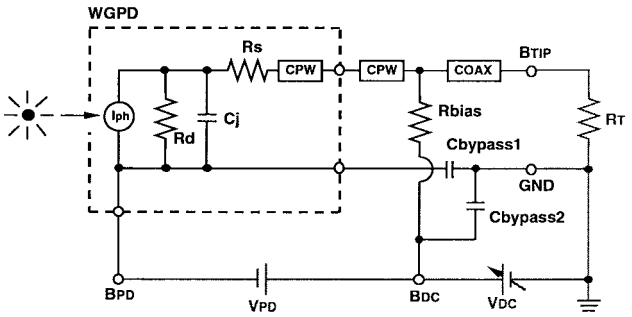

Fig. 2. Equivalent circuit of the Type-I probe head. The portion blocked by the dashed line corresponds to the WGPD, and drawings with shaded lines indicates the setup for connections of external dc power supplies and the DUT.

employ a 1.55-μm 85-GHz bandwidth WGPD. The Type-I probe is an improved version of the first trial probe. It employs a simple semirigid coaxial cable with a bias network for the electrical-signal transmission, resulting in a very low modal dispersion of $<$1.0 ps over a bandwidth of 100 kHz to 60 GHz. The Type-II probe newly employs a broad-band InP high electron-mobility transistor (HEMT) distributed amplifier that boosts the electrical output signal amplitude over 1 V peak to peak with a bandwidth of 100 kHz to near 40 GHz.

II. Structure of OE Probe

A. Type-I Probe

Fig. 1 shows a schematic of the Type-I optoelectronic active stimulus probe head. Optical beams coming from the fiber concentric connection with standard physical contact (FC/PC) connector are introduced to a single mode fiber. A pair of optical lenses collimates and focuses the beams onto the side edge of the photo absorption layer of a 1.55-μm WGPD. This lens-based rigid assembly allows good reproducibility against overdriving stresses that arise when the probe tip is contacted to the device under measurement. The WGPD employs a novel multimode optical waveguide structure with doped InGaAsP intermediate-bandgap layers between the InGaAs core layer and the InP clad layers [16]. This permits waveguide multimode propagation resulting in a high external quantum efficiency of 60% or 0.75 A/W. The optical waveguide has a mushroom-mesa structure [16] providing a 85-GHz bandwidth. The WGPD output is introduced to a 400-μm-long CPW on the InP substrate followed by a short-length (1.5 mm) CPW transformer on an Al_2O_3 substrate with silver epoxy adhesive, and then connected to a 1-mm-diameter 25-mm-long semirigid coaxial cable (coax). The far end of the coax is formed as an air-coplanar probe tip. This coax-based structure provides modal-dispersion-free transmission from dc to 125 GHz (the cutoff frequency of the coax).

The bias network, which provides the dc bias for the WGPD and the probe tip, was implemented with a resistor and bypass capacitor. Its equivalent circuit, including the WGPD, are shown in Fig. 2. The equivalent-circuit parameters for the WGPD were R_d, junction resistance, C_j, junction capacitance, R_s, series resistance, and $I_{\rm ph}$, photogenerated current. The dc bias port $B_{\rm DC}$ has a role to provide a dc bias to the probe tip and is connected to the WGPD output node via a 384-Ω chip-resistor ($R_{\rm bias}$) instead of an inductor. The resistive biasing improves undesired gain ripple at low frequencies caused by LC resonance, although the bias voltage is offset according to the load impedance (R_T) at the probe tip ($B_{\rm TIP}$). To decouple the cathode electrode (power-supply port $B_{\rm PD}$) of the WGPD from the dc ground of the tip (GND), the bypass capacitor $C_{\rm bypass1}$ is inserted between ground patterns of the alumina CPW transformer and that of the semirigid coax. The dc bias (reverse bias) for the WGPD is supplied to the port $B_{\rm PD}$ as an offset from the port $B_{\rm DC}$ so that a weak dc photodiode (PD) current goes through $B_{\rm DC}$ to $B_{\rm PD}$. Compared to the prior art [16] in which the bypass capacitor and an inductor are implemented on the RF signal path to supply an independent dc bias to the PD, the gain flatness of the RF signal line has been improved, although the dc-biasing procedure for the PD must follow a few relatively complicated steps and an input dc resistance of the DUT must be known beforehand. The value of the decoupling capacitor $C_{\rm bypass1}$ determines the lower cutoff frequency of the electrical circuit. We put 0.2-μF of ferroelectric capacitor plates and microchip capacitors as $C_{\rm bypass1}$ to assure a lower cutoff frequency of less than 200 kHz.

To show how the tip and the WGPD are dc biased, Fig. 2 also shows the setup for connections of external dc power supplies and the DUT with shaded lines. Here, we assume that the probe tip ($B_{\rm TIP}$) is to be biased at $V_{\rm bias}$ and the WGPD is to be intrinsically biased at $V_{\rm pd}$ and that the DUT has an input dc resistance of R_T. Biasing the WGPD and probe tip requires the following procedures: 1) bias the port $B_{\rm DC}$ (from the GND) to

$$V_{\rm DC} = [(R_T + R_{\rm bias})/R_T]V_{\rm bias}$$

and 2) bias the port $B_{\rm PD}$ (offset from the port $B_{\rm DC}$) to

$$V_{\rm PD} = V_{\rm pd} - [R_{\rm bias}/(R_{\rm bias} + R_T)]V_{\rm DC}.$$

The S-parameters of the electrical-signal transmission line without the WGPD chip were measured before assembling the WGPD. The measured $-$3-dB bandwidth was 100 kHz to 94 GHz. A good return loss of less than $-$10 dB was also obtained in this frequency range.

B. Type-II Probe

As shown in Fig. 1, the Type-II probe newly employs a broad-band InP HEMT distributed amplifier IC in order to

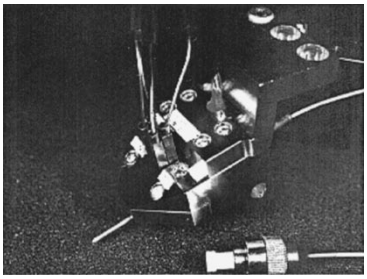

(a)

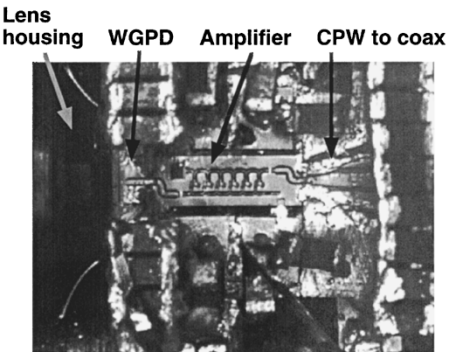

(b)

Fig. 3. (a) Appearance of OE probe. (b) Microphotograph of the distributed amplifier IC assembled in the Type-II probe.

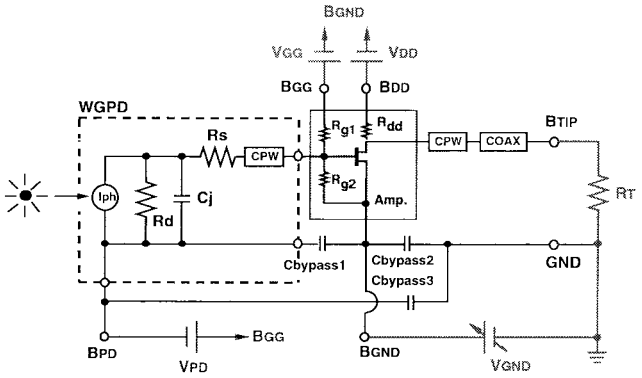

Fig. 4. Equivalent circuit of the Type-II probe head. The portion blocked by the dashed line corresponds to the WGPD and the shaded area shows the amplifier IC. Drawings with shaded lines indicate the setup for connections of external dc power supplies and the DUT.

boost the electrical output signal amplitude over 1 $V_{p\text{-}p}$. This is essential for applications to high-speed digital IC testing, where most circuits operate with near 1-$V_{p\text{-}p}$ input/output interfaces. Its structure is basically the same as that of Type I, except that the amplifier is inserted between the WGPD and CPW transformer. A microphotograph of the probe assembly is shown in Fig. 3, and an equivalent circuit of the probe is shown in Fig. 4. The resistances R_{dd}, R_{g1}, and R_{g2} are internal bias resistors of the amplifier IC. The WGPD output (CPW on an InP substrate) is directly connected to the amplifier input CPW with Au ribbon wire. The output CPW of the amplifier is introduced to the CPW transformer on an Al_2O_3 substrate to connect to the semirigid coax. The ground plane of the InP CPW is decoupled from the amplifier ground plane via ferroelectric capacitor plates and microchip capacitors ($C_{\rm bypass1}$), and the amplifier ground ($B_{\rm GND}$) is decoupled by $C_{\rm bypass2}$ from the dc ground of the tip (GND) so that the dc bias of the tip may be controlled by offsetting the dc bias at $B_{\rm GND}$ from GND appropriately. The values for $C_{\rm bypass1}$ and $C_{\rm bypass2}$ were the same as that of $C_{\rm bypass1}$ in the Type-I probe. The dc bias (reverse bias) for the WGPD is supplied to the port $B_{\rm PD}$ as an offset from the port $B_{\rm GG}$ so that a weak dc PD current goes through $B_{\rm GG}$ to $B_{\rm PD}$.

To show how the tip and WGPD are dc biased, Fig. 4 also shows the setup for connections of external dc power supplies and the DUT with shaded lines. Here, we assume that: 1) the probe tip ($B_{\rm TIP}$) is to be biased at $V_{\rm bias}$ and the WGPD is to be intrinsically biased at $V_{\rm pd}$, 2) the amplifier IC normally operates with a dc current flow I_{dd} and a dc bias $V_{\rm ds}$ from the output node to the amplifier ground $B_{\rm GND}$, and 3) the DUT has an input dc resistance of R_T. Biasing the WGPD and the probe tip requires the following procedures.

1) Bias the port $B_{\rm GND}$ (from GND) to
$$V_{\rm GND} = V_{\rm bias} - V_{\rm ds}.$$
2) Bias the port $B_{\rm DD}$ (from the $B_{\rm GND}$) to
$$V_{\rm DD} = (1 + R_{dd}/R_T)V_{\rm bias} + R_{dd}I_{dd}.$$
3) Bias the port $B_{\rm GG}$ (from the $B_{\rm GND}$) to a specific level $V_{\rm GG}$ according to the amplifier specification so as to make the amplifier operate normally.
4) Bias the port $B_{\rm PD}$ (offset from the port $B_{\rm GG}$) to
$$V_{\rm PD} = V_{\rm pd} - [R_{g1}/(R_{g1} + R_{g2})]V_{\rm GG}.$$

Fig. 5 shows the circuit diagram of the HEMT amplifier. The distributed amplifier has a 50-Ω input impedance to match the characteristic impedance of the CPW on the WGPD. The amplifier consists of six-section cascode amplifier cells. Their input and output nodes are serially connected with artificial transmission lines and are terminated with impedance-matched resistors so as to perform velocity-matched traveling-wave signal amplification between the input and output transmission lines [18]. The input and output terminations are constructed with dc matching terminations and dumping resistors [18] to achieve a flat gain starting from 0 Hz and to reduce the parasitic effects of external inductances at the bias terminals. The cascode connection of HEMT's in the amplifier cell is to reduce the influence of the Miller capacitance and can compensate for frequency rolloff loss, resulting in the increase in bandwidth [19]. For the common-gate HEMT, a self-bias circuit is configured with a gate–drain feedback resistance and two series diodes. Loss compensation circuitry [18] was also implemented to enhance the bandwidth of the amplifier, in which two artificial transmission lines (L_{sd} and L_{cg}) are inserted in the amplifier cell to compensate for the output-line loss at high frequencies [18]. The transconductance (G_m), current–gain cutoff frequency (f_T), and unilateral-gain cutoff frequency ($f_{\rm max}$) of the HEMT's are 1.0 S/mm, 174 GHz, and 200 GHz, respectively. The typical dc gain and $-$3-dB bandwidth of the fabricated chip are 11 dB and 87 GHz, respectively. The saturated output level at 1-dB compression is $+$5.6 dBm. The maximally rated dc current at the output port

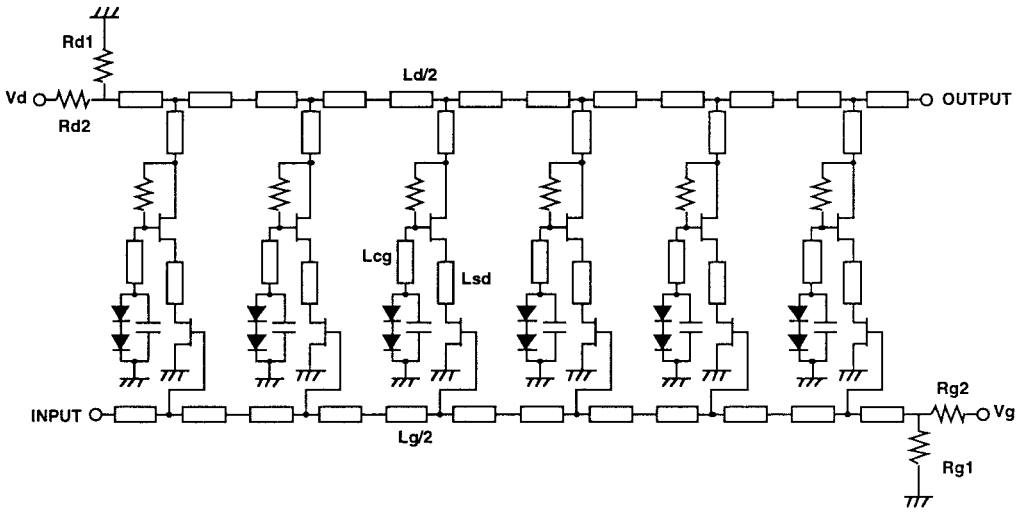

Fig. 5. Circuit diagram of HEMT distributed amplifier IC.

is 20 mA. This means the probe tip can be dc-offset within ± 1 V under the 50-Ω termination condition.

The S-parameters of the electrical-signal transmission line (from the input pad of the amplifier to the probe tip) was measured before assembling the WGPD. The measured dc gain was $+9$ dB, and the -3-dB bandwidth was 100 kHz to 90 GHz. A good return loss of less than -10 dB was also obtained in this frequency range.

III. Experiment

A. Measurement Setup

For fabricated Type-I and Type-II probe heads, impulse response measurement was conducted by a pump-probe technique using electrooptic sampling (EOS). The measurement setup is shown in Fig. 6(a). The probe tip was contacted to the near end of a 50-Ω CPW on a GaAs substrate with the far end terminated. The GaAs substrate was also utilized as an electrooptic transducer. The electric field close to the contact pad of the OE probe was detected using the back illuminated direct sampling scheme [20]. An adiabatically compressed soliton pulse with a 750-fs full width at half maximum (FWHM) and a 500-MHz repetition was used as the pump and probe pulse [21], which is generated in the optical pulse generator block. The pump pulse power or the peak height of the pump pulse was controlled using an optical variable attenuator in order to measure the dependence of the probe response on incident pulse power. It was confirmed beforehand that the pump pulse shape was not affected by its peak height. After the impulse response measurement, the response to several practical optical pulse-pattern streams (generated in the electrooptic pulse-pattern generator block) was also measured with synchronization sampling using a high-repetition-rate ($\sim$9 GHz) soliton pulse, as shown in Fig. 6(b).

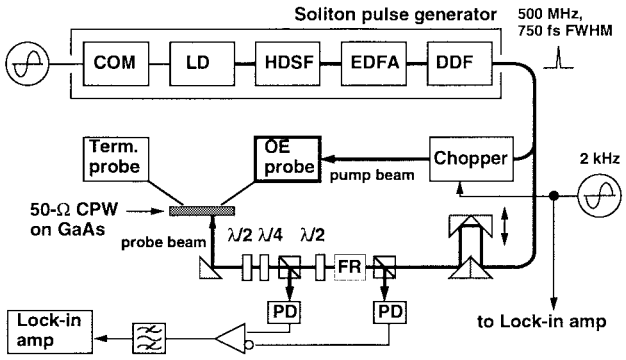

(a)

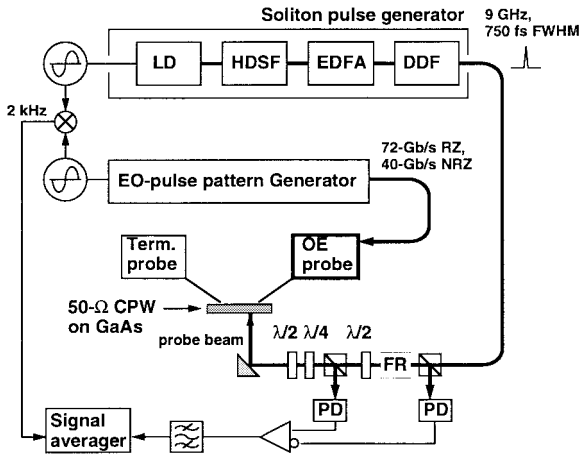

(b)

Fig. 6. Optoelectronic measurement setup. (a) Impulse response measurement. (b) Pulse-pattern response measurement. COM: comb generator, LD: laser diode, HDSF: highly dispersion-shifted fiber, EDFA: erbium-doped fiber amplifier, DDF: dispersion-decreasing fiber, FR: Faraday rotator, and PD: photodiode.

B. Type-I Probe

Typical measured output waveforms and pulsewidths are shown in Fig. 7(a) and (b), respectively. When the incident average power attenuated to 20 μW, an average photocurrent of 15 μA was obtained, which implies a responsivity of 0.75 A/W. The output waveform shows a good symmetrical response, except for small side peaks caused by multiple reflection. The pulsewidth slightly decreased with increasing

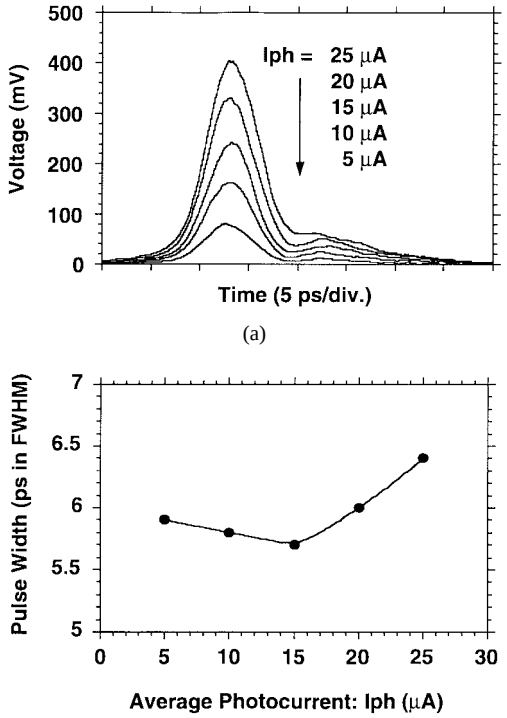

Fig. 7. Measured impulse response of the Type-I probe. (a) Output waveforms for 750-fs FWHM incident pulses with various power levels. (b) Pulsewidth in FWHM.

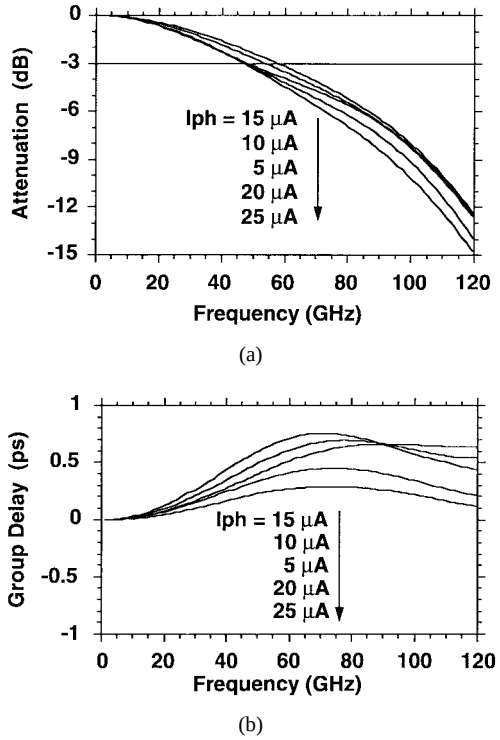

Fig. 8. Frequency response of the Type-I probe calculated using FFT from the results in Fig. 7. (a) Attenuation. (b) Group delay.

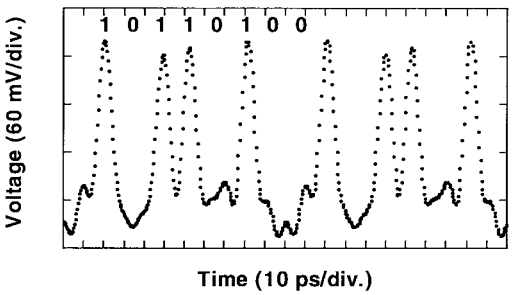

Fig. 9. Measured output waveform of the Type-I probe for a 72-Gbit/s RZ mode, "10110100 ⋯" repetitive pattern.

average photocurrent up to 15 μA. At this point, a minimum pulsewidth of 5.7-ps FWHM with an output voltage of 240 $mV_{p\text{-}p}$ was obtained, which is 30% faster than that of the conventional model [16]. The pulsewidth gradually increased with further increases in incident signal power. When the average photocurrent becomes 25 μA, the pulsewidth widened to 6.4-ps FWHM and output saturation became evident. 1-dB compression output voltage was 400 $mV_{p\text{-}p}$ at the probe tip.

The frequency response was calculated using fast Fourier transform (FFT). Note that the incident optical pulse has a repetition rate of 500 MHz, so the frequency response that can be calculated is beyond 500 MHz. The effect of bandwidth limitation ($\sim$750-fs FWHM) of the pump and probe pulses were deconvolved assuming an ideal hyperbolic-secant-soliton pulse shape. For simplicity, the gain and phase of the fundamental frequency component (500 MHz) were normalized to be 0 dB and 0 ps, respectively. This treatment, however, is valid for estimating the $-$3-dB bandwidth and the group-delay dispersion. The results are shown in Fig. 8. The highest $-$3-dB bandwidth was 60 GHz at an output voltage of 250 $mV_{p\text{-}p}$ (an average photocurrent of 15 μA). The calculated group-delay dispersion was no more than 0.8 ps at frequencies below 100 GHz, and near dispersion-free response was obtained over the bandwidth.

The response to a 72-Gbit/s return-to-zero (RZ) repetitive pattern "10110100 ⋯" was observed. The incident optical pulse pattern was generated using an electrooptic pulse-pattern generator [17], [22]. The pulsewidth of the generated signal was 4.9-ps FWHM. The result is shown in Fig. 9. A clear 72-Gbit/s RZ electrical signal was observed from the probe tip, although the pulsewidth is enlarged and extinction is slightly degraded. The extinction at this rate is far better than that for the conventional CPW-based OE probe at 64 Gbit/s. This is mostly owing to the improvement of the modal frequency dispersion along the electrical transmission line.

C. Type-II Probe

Typical measured output waveforms and pulsewidths are shown in Fig. 10(a) and (b), respectively. The minimum pulsewidth of 8.3-ps FWHM with an output voltage of 530 $mV_{p\text{-}p}$ is obtained when the average photocurrent (I_{ph}) is 15 μA. The pulsewidth gradually increases to 9.2 ps with increasing I_{ph} to 30 μA. The 1-dB compression output voltage and saturation voltage are 820 and 1000 $mV_{p\text{-}p}$, respectively. Introduction of the wide-band amplifier successfully improved the conversion efficiency and output saturation voltage.

The output waveform shows a slightly asymmetrical response with side peaks, which is caused by the amplifier. The details will be discussed later. The frequency response

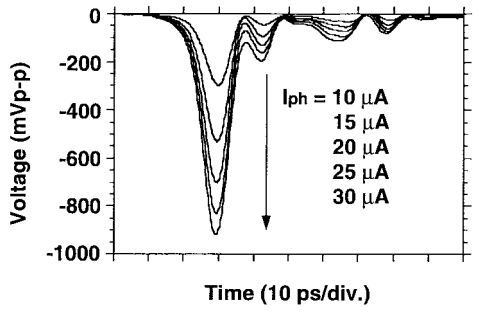

(a)

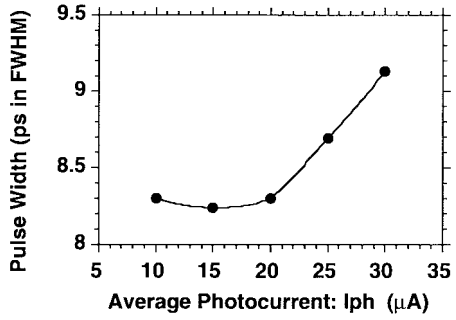

(b)

Fig. 10. Measured impulse response of the Type-II probe. (a) Output waveforms for 750-fs FWHM incident pulses with various power levels. (b) Pulsewidth in FWHM.

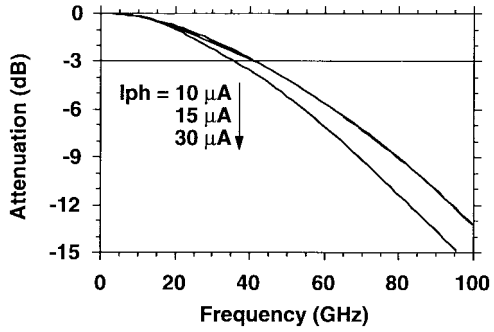

(a)

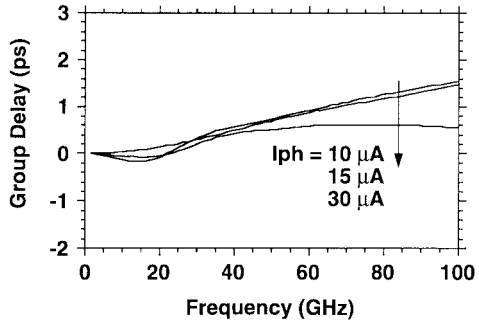

(b)

Fig. 11. Frequency response of the Type-II probe calculated using FFT from the results in Fig. 10. (a) Attenuation. (b) Group delay.

was calculated using FFT. The results are shown in Fig. 11. The effective −3-dB bandwidth is 40 GHz when $I_{\rm ph}$ is below 15 μA (corresponding to an output voltage of below 530 $\rm mV_{p\text{-}p}$), and is 35 GHz when $I_{\rm ph}$ is increased to 30 μA (an output voltage of 930 $\rm mV_{p\text{-}p}$). The calculated group-delay dispersion is no more than 1.6 ps at frequencies below 100 GHz.

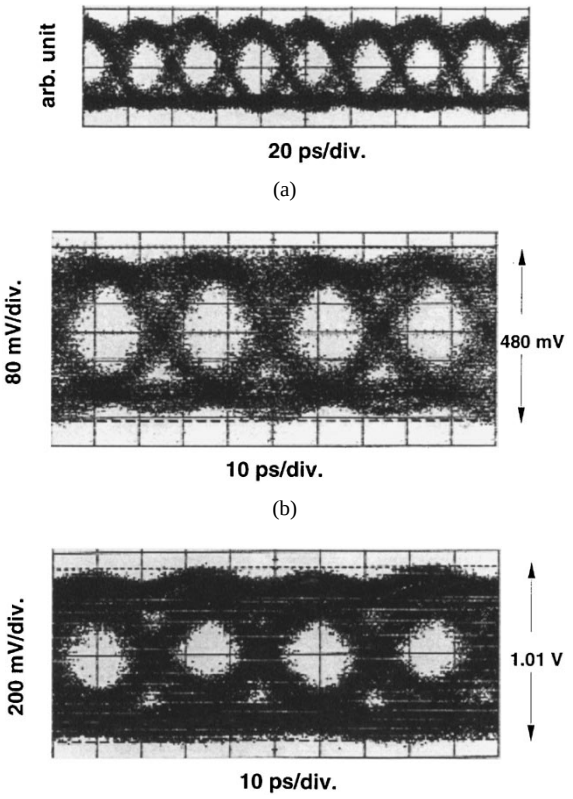

Fig. 12. Measured output waveform of the Type-II probe for a 40-Gbit/s NRZ-mode pseudorandom pattern. (a) Input. (b) 480-mV output. (c) 1.01-V output.

The response to a 40-Gbit/s nonreturn-to-zero (NRZ) pseudorandom pattern was observed. The incident optical pulse pattern was generated using an electrooptic pulsation technique [20]. The results are shown in Fig. 12. Clear 40-Gbit/s, NRZ electrical signals with voltage swings up to 1 $\rm V_{p\text{-}p}$ were obtained from the probe head, although the eye-opening was slightly degraded by increasing the voltage swing.

IV. Discussion

In the results of impulse response measurements for both Type-I and Type-II probes, ringing with a main satellite pulse 10 ps after the first pulse was observed. It is thought that this is due to multiple reflection between the PD output and CPW far end on the InP substrate. This is because the PD output impedance was not matched to 50 Ω. Adding to the equivalent circuit for the WGPD shown in Fig. 2, the bandwidth limitation along with the electrical transmission line, including discontinuities at the CPW connection (InP CPW to Al_2O_3 CPW and Al_2O_3 CPW to coax) was simply modeled, and then the impulse response for the Type-I probe was simulated. The CPW's on the InP and Al_2O_3 substrate were modeled as 50-Ω transmission lines with a monotonic loss of 0.5 and 1.6 dB at 100 GHz, an electrical delay of 4.7 and 13.5 ps, and a linear group-delay dispersion of +0.3 and +0.9 ps at 100 GHz, respectively. The coax was

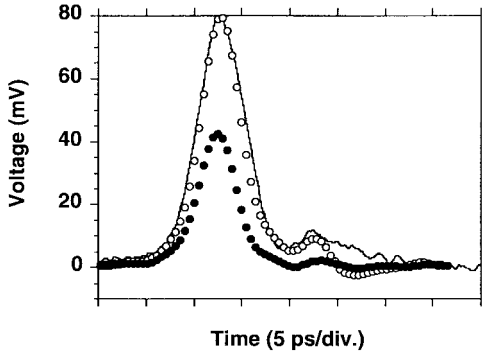

Fig. 13. Simulated impulse response of the Type-I probe (open circles). The solid circles are results in the case of a 50-Ω matched termination condition at the WGPD output. The solid line is the measured result.

modeled as a 50-Ω transmission line with a monotonic loss of 1.5 dB at 100 GHz and with an electrical delay of 100 ps. The equivalent-circuit parameters for the WGPD were: $R_d = 100\ \mathrm{M}\Omega$, $C_j = 20.3$ fF, and $R_s = 10\,\Omega$. According to [24], it is well assumed for high-speed p-i-n PD's that the intrinsic (or active) layer thickness is far less than the inverse absorption coefficient and that an appropriate reverse-bias condition can makes the intrinsic layer fully depleted and makes carriers travel at the saturation velocity during most of the transit. Consequently, the photocurrent $i_{\mathrm{pd}}(t)$ for uniform and instant illumination at $t = 0$ to the WGPD was approximated as

$$\begin{aligned} i_{\mathrm{pd}}(t) &= i_e(t) + i_h(t) \\ i_e(t) &= qnAv_e/d(1 - v_e/dt), \qquad 0 \le t \le d/v_e \\ &= 0, \qquad t < 0,\ t > d/v_e \\ i_h(t) &= qnAv_h/d(1 - v_h/dt), \qquad 0 \le t \le d/v_h \\ &= 0, \qquad t < 0,\ t > d/v_h \end{aligned}$$

where q is the electron charge, n the photogenerated electron–hole pair density at $t = 0$, A the effective junction area, v_e and v_h the saturation velocity for electrons and holes, and d the active layer thickness. We assumed a d of 0.2 μm, a v_e of 6.5 $\times$ 10^4 m/s, and a v_h of 4.8 $\times$ 10^4 m/s.

When the characteristic impedance at the contact between InP CPW and Al_2O_3 CPW was assumed to be 65 Ω, the simulated results expressed the satellite pulse in measured waveforms well, as shown in Fig. 13. It also suggests that when a 50-Ω matched resistor is incorporated, the satellite pulse peak can be suppressed below 1% as short as the main pulse height even though the output signal amplitude is sacrificed to be a half. Recently developed unitraveling-carrier PD's with extremely high output saturation characteristics will have the potential to enhance the probe output saturation beyond 1 $V_{\mathrm{p\text{-}p}}$ even under the 50-Ω matched condition [23].

The response speed of the Type-I probe depends on the average photocurrent (or optical input power), as shown in Fig. 7(b). When the average photocurrent is low, the response is rather slow and becomes slightly faster with increasing the input power up to the minimum point. The optically excited carriers will perturb the conductivity at the intrinsic layer edge and then the depletion layer thickness, which may affect both

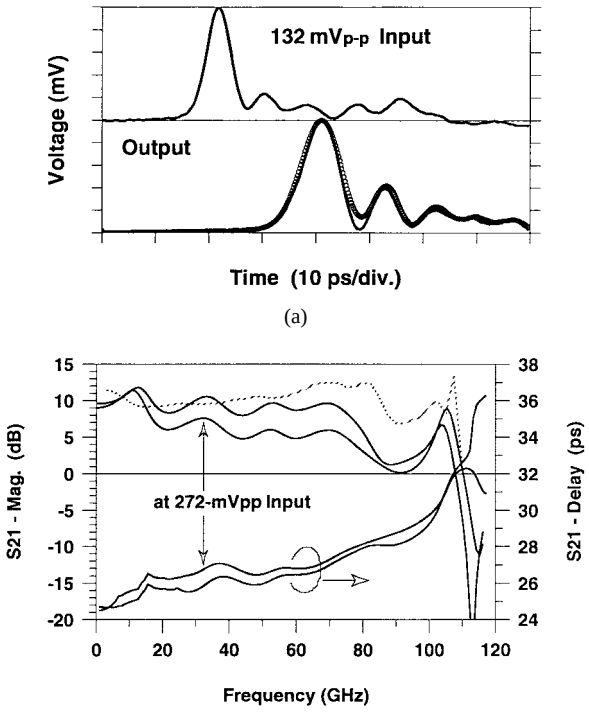

Fig. 14. The impulse response of the HEMT distributed amplifier IC used in the Type-II probe. (a) Upper: 132-$mV_{p\text{-}p}$ 6.0-ps FWHM input pulse injected using the Type-I probe, lower: output waveforms for an incident pulse with 132 $mV_{p\text{-}p}$ (solid line) and with 272 $mV_{p\text{-}p}$ (open circles). (b) Calculated frequency response. The dashed line shows the result of the small-signal vector network measurement. The solid lines are the FFT results for 132- and 272-$mV_{p\text{-}p}$ incident pulses.

the parellel-capacitance series-resistance product (CR) time constant and carrier transit time. It should be quantitatively analyzed. When the input power becomes higher, excess carrier inside the depletion region reduce the electric field, which increases the carrier transit time resulting in pulsewidth broadening [25].

The response speed of the Type-II probe also has a similar dependence on optical input power, but the probe bandwidth is further limited than is expected from the PD response when the incident power increases over the fastest response level. The amplifier bandwidth was then measured for several input power conditions by means of the pump-probe technique. The Type-I probe was used for electrical impulse injection to the amplifier. The measured time-domain responses are shown in Fig. 14(a). The upper trace shows a 132-$mV_{p\text{-}p}$ 6.0-ps FWHM input pulse injected using the Type-I probe. The lower traces show typical output waveforms for an incident pulse with 132 $mV_{p\text{-}p}$ (solid line) and with 272 $mV_{p\text{-}p}$ (open circles). For a large incident pulse with 272 $mV_{p\text{-}p}$, we see a dull transition at the falling edge.

Fig. 14(b) shows calculated frequency responses. The solid lines are the FFT results for 132- and 272-$mV_{p\text{-}p}$ incident pulses. For comparison, the S_{21} magnitude obtained by the small-signal vector network measurement is plotted by the dashed line. The calculated bandwidth clearly exhibits the saturation characteristics of the amplifier. When the input pulse height is 132 $mV_{p\text{-}p}$, the calculated -3-dB bandwidth

is 82 GHz. This value is slightly lower than the result (87 GHz) of the small-signal vector network measurement. The bandwidth reduces to 40 GHz when the input pulse height becomes 272 $mV_{p\text{-}p}$. The group delay dispersion was 4 ps at 100 GHz. Thus, the asymmetrical waveform measured for the Type-II probe is mostly caused by the amplifier dispersion. The overall probe bandwidth calculated using the measured results for each component (82 GHz for the amplifier and others equivalent to those for a Type-I probe) was 47 GHz, which is wider than the experimental result of 40 GHz. The major cause is thought to be the multiple reflection between the PD output and amplifier input because of the unmatched output impedance of the PD.

It is also noted that the frequency response of the amplifier calculated from the impulse response exhibits steep cutoff characteristics at 108 GHz, which coincides well to the small-signal vector network measurement. Therefore, an effective measurement bandwidth of the Type-I probe exceeds 100 GHz and is close to the cutoff frequency (125 GHz) of the coax inside the probe when the probe is utilized in a pump-probe measurement.

V. Conclusion

Two types of wide-band high-efficiency OE conversion stimulus probe heads were developed for testing large-signal responses of high-speed electronic devices. Both of them employed a 1.55-μm 85-GHz bandwidth WGPD. The Type-I probe employed a simple semirigid coaxial cable with a bias network for the electrical-signal transmission to reduce the modal frequency dispersion. The measured results assured a good symmetrical impulse response with a very low modal dispersion of $<$1.0 ps. The highest $-$3-dB bandwidth of 60 GHz was obtained for an output voltage of 250 $mV_{p\text{-}p}$, and was maintained beyond 50 GHz for output voltages of up to 400 $mV_{p\text{-}p}$. The Type-I probe successfully converted a 72-Gbit/s RZ optical pulse pattern to an electrical pattern with a good extinction. The Type-II probe employed a broad-band InP HEMT distributed amplifier that boosts the electrical output signal amplitude over 1 V peak to peak. The $-$3-dB bandwidth was 40 (35) GHz for output voltages up to 500 (1000) mV peak to peak. The Type-II probe converted an optically generated 40-Gbit/s NRZ pseudorandom pulse to a 1-$V_{p\text{-}p}$ swing electrical pulse with a good eye opening. Currently the probe head bandwidth is mainly limited by worse return characteristics of the PD output. 50-Ω matching of the PD output impedance should be introduced for further speed improvement even though the output voltage swing is sacrificed.

Acknowledgment

The authors thank S. Horiguchi, H. Yoshimura, J. Yoshida, O. Karatsu, E. Sano, O. Nakajima, and K. Matsuhiro for their direction and encouragement. They also thank M. Yaita and M. Yoneyama for their experimental support and valuable discussions.

References

[1] S. Kimura, Y. Imai, Y. Umeda, and T. Enoki, "0–90 GHz InAlAs/InGaAs/InP HEMT distributed baseband amplifier IC," *Electron. Lett.*, vol. 31, no. 17, pp. 1430–1431, 1995.

[2] T. Otsuji, K. Murata, T. Enoki, and Y. Umeda, "An 80-Gbit/s multiplexer IC using InAlAs/InGaAs/InP HEMT's," in *Proc. IEEE GaAs IC Symp.*, Anaheim, CA, 1997, pp. 183–186.

[3] J. A. Valdmanis, J. A. Mourou, and C. W. Gabel, "Subpicosecond electrooptic sampling," *IEEE J. Quantum Electron.*, vol. QE-19, pp. 664–667, Apr. 1983.

[4] K. J. Weingarten, M. J. Rodwell, and D. M. Bloom, "Picosecond optical sampling of GaAs integrated circuits," *IEEE J. Quantum Electron.*, vol. 24, pp. 198–220, Feb. 1988.

[5] M. Y. Frankel, J. F. Whitaker, and G. A. Mourou, "Optoelectronic transient characterization of ultrafast devices," *IEEE J. Quantum Electron.*, vol. 28, pp. 2313–2324, Oct. 1992.

[6] T. Nagatsuma, "Measurement of high-speed devices and integrated circuits using electro-optic sampling techniques," *IEICE Trans. Electron.*, vol. E76-C, no. 1, pp. 55–63, 1993.

[7] D. H. Auston, "Picosecond optoelectronic switching and gating in silicon," *Appl. Phys. Lett.*, vol. 26, pp. 101–103, 1975.

[8] P. R. Smith, D. H. Auston, and W. M. Augyniak, "Measurement of GaAs field-effect transistor electronic impulse response by picosecond optical electronics," *Appl. Phys. Lett.*, vol. 39, no. 9, pp. 739–741, 1981.

[9] H.-L. A. Hung, P. Polak-Dingels, K. J. Webb, T. Smith, H.C. Huang, and C. H. Lee, "Millimeter-wave monolithic integrated circuit characterization by a picosecond optoelectronic technique," *IEEE Trans. Microwave Theory Tech.*, vol. 37, pp. 1223–1231, Aug. 1989.

[10] S. L. Huang, E. A. Chauchard, C. H. Lee, T. T. Lee, H.-L. A. Hung, and T. Joseph, "On-wafer testing of MMIC with monolithically integrated photoconductive switches," in *IEEE MTT-S Int. Microwave Symp. Dig.*, 1992, pp. 661–664.

[11] M. D. Feuer, S. C. Shunk, P. R. Smith, M. C. Nuss, and H. H. Law, "100-GHz wafer probes based on photoconductive sampling," *IEEE Photon. Technol. Lett.*, vol. 5, pp. 361–364, Mar. 1993.

[12] J. Nees and S. Williamson, "Picosecond detector, optical temporal analyzer, and free-standing circuit probe," in *Proc. Ultrafast Electron. Optoelectron.*, 1993, pp. 24–26.

[13] T. Pfeifer, H.-M. Heiliger, E. S. Kamienski, H. G. Roskos, and H. Kurz, "High-frequency on-wafer testing with freely positionable silicon-on-sapphire photoconductive probes," in *IEEE MTT-S Int. Microwave Symp. Dig.*, 1995, pp. 1053–1056.

[14] A. Deutsch, M. R. Scheuermann, G. Arjavalingam, L. Kneller, J. K. Tam, and C. W. Surovic, "Characterization of resistive transmission lines to 70 GHz with ultrafast optoelectronics," *IEEE Microwave Guided Wave Lett.*, vol. 3, pp. 75–77, Mar. 1993.

[15] T. Otsuji, K. Kato, T. Nagatsuma, and M. Yoneyama, "10–72-Gb/s, optoelectronic RZ pulse-pattern generation and its application to on-wafer large-signal characterization for ultrahigh-speed electronic devices," in *Proc. IEEE LEOS Annu. Meeting*, 1994, pp. 203–204.

[16] ——, "50-GHz bandwidth, 0.75-A/W optoelectronic stimulus probe head employing multimode waveguide p-i-n photodiode," *IEEE Photon. Technol. Lett.*, vol. 8, pp. 411–413, Mar. 1996.

[17] ——, "Widely tunable electrooptic pulse-pattern generation and its application to on-wafer large-signal characterization of ultra high-speed electronic devices," *Opt. Quantum Electron.*, vol. 28, no. 7, pp. 991–1005, 1996.

[18] S. Kimura, Y. Imai, Y. Umeda, and T. Enoki, "Loss-compensated distributed baseband amplifier IC's for optical transmission systems," *IEEE Trans. Microwave Theory Tech.*, vol. 44, pp. 1688–1693, Oct. 1996.

[19] S. Deibele and J. B. Beyer, "Attenuation compensation in distributed amplifier design," *IEEE Trans. Microwave Theory Tech.*, vol. 37, pp. 1425–1433, Sept. 1989.

[20] T. Nagatsuma, T. Otsuji, N. Shimizu, M. Yaita, K. Kato, and M. Shinagawa, "Optoelectronic techniques for characterization of millimeter-wave devices," in *Proc. IEEE MTT-S & LEOS Topical Meeting Opt. Microwave Interactions*, 1994, pp. 7–8.

[21] T. Nagatsuma, M. Yaita, M. Shinagawa, K. Kato, A. Kozen, K. Iwatsuki, and K. Suzuki, "Electrooptic characterization of ultrafast photodetectors using adiabatically compressed soliton pulses," *Electron. Lett.*, vol. 30, no. 10, pp. 814–815, 1994.

[22] T. Otsuji, M. Yaita, T. Nagatsuma, and E. Sano, "10–80-Gbit/s, highly extinctive electrooptic pulse pattern generation," *IEEE J. Select. Topics Quantum Electron.*, vol. 3, pp. 643–649, Mar. 1996.

[23] T. Ishibashi, N. Shimizu, S. Kodama, H. Ito, T. Nagatsuma, and T. Furuta, "Uni-traveling-carrier photodiodes," in *Ultrafast Electron. Optoelectron. Tech. Dig.*, vol. UWA2, 1997, pp. 166–168.
[24] J. E. Bowers and C. A. Burrus, Jr., "Ultrawide-band long-wavelength p-i-n photodetectors," *J. Lightwave Technol.*, vol. LT-5, pp. 1339–1350, Oct. 1987.
[25] Y. G. Wey, K. Giboney, J. Bowers, M. Rodwell, P. Silvestre, P. Thiagarajan, and G. Robinson, "110-GHz GaInAs/InP double heterostructure p-i-n photodetectors," *J. Lightwave Tech.*, vol. 13, pp. 1490–1499, July 1995.

Taiichi Otsuji (M'91) was born in Fukuoka, Japan, on September 5, 1959. He received the B.S. and M.S. degrees in electronic engineering from Kyushu Institute of Technology, Fukuoka, Japan, in 1982 and 1984, respectively, and the Ph.D. degree in electronic engineering from the Tokyo Institute of Technology, Tokyo, Japan, in 1994.

In 1984, he joined the Electrical Communication Laboratories, Nippon Telegraph and Telephone Corporation (NTT), Japan, where he was engaged in the research and development of high-speed large scale integration (LSI) test systems. He was a Senior Research Engineer, Supervisor at the Network Innovation Laboratories, NTT, Kanagawa, Japan. He is currently an Associate Professor in the Department of Control Engineering and Science, Kyushu Institute of Technology, Fukuoka, Japan. His current research interest includes ultra-broad-band electronic IC design and ultrafast optoelectronic measurement technologies.

Dr. Otsuji is a member of the Institution of Electronics, Information and Communication Engineers (IEICE), Japan, and the Optical Society of America (OSA). He was the recipient of the Outstanding Paper Award presented at the 1997 IEEE GaAs IC Symposium.

Kazutoshi Kato (A'91–M'93) received the B.S. and M.S. degrees in physics and the Ph.D. degree from Waseda University, Tokyo, Japan, in 1985, 1987, and 1993, respectively.

Since 1987, he has been with Nippon Telegraph and Telephone Corporation (NTT) Opto-Electronics Laboratories, Kanagawa, Japan, where he was engaged in research on receiver optoelectronic IC's (OEIC's) and high-speed p-i-n photodetectors. From 1994 to 1995, he was on leave from NTT, working on metal–semiconductor–metal (MSM) photodetectors at France Telecom CNET Bagneux Laboratory, France, for one year. His current activities focus on photoreceivers for wide-band transmissions, microwave applications, and optical access networks.

Dr. Kato is a member of the Institute of Electronics, Information and Communication Engineers (IEICE), Japan, the Japan Society of Applied Physics, and the IEEE Lasers and Electro-Optics Society (LEOS).

Shunji Kimura (M'92) was born in Tokyo, Japan, on January 28, 1967. He received the B.S. and M.S. degrees in electrical engineering and the Ph.D. degree in electronics, information, and communication engineering from Waseda University, Tokyo, Japan, in 1989, 1991, and 1997, respectively.

In 1991, he joined the LSI Laboratories, Nippon Telegraph and Telephone Corporation (NTT), Kanagawa, Japan. He is currently assigned to the NTT Network Innovation Laboratories, Kanagawa, Japan. He has been engaged in design and evaluation of microwave and millimeter-wave monolithic IC's for high-speed optical transmission systems.

Dr. Kimura is a member of the Institute of Electronics, Information and Communication Engineers (IEICE), Japan, and the Physical Society of Japan. He was the recipient of the Japan Microwave Prize presented at the 1994 Asia–Pacific Microwave Conference and the 1996 Young Engineer Award given by the IEICE.

Tadao Nagatsuma (M'93) received the B.S., M.S., and Ph.D. degrees in electronic engineering from Kyushu University, Fukuoka, Japan, in 1981, 1983, and 1986, respectively.

He joined the Electrical Communications Laboratories, Nippon Telegraph and Telephone Corporation (NTT), Kanagawa, Japan, in 1986. He is currently a Senior Research Engineer, Supervisor at NTT Telecommunications Energy Laboratories, Kanagawa, Japan. His current research involves design, characterization, and testing of high-speed semiconductor devices and IC's, and ultrafast optoelectronics.

Dr. Nagatsuma is a member of the Optical Society of America (OSA), the Japan Society of Applied Physics, and the Institute of Electronics, Information and Communication Engineers (IEICE), Japan. He was the recipient of the 1989 Young Engineers Award presented by the IEICE, the 1992 IEEE Andrew R. Chi Best Paper Award, the 1997 Okochi Memorial Award, and the Japan Microwave Prize presented at the 1998 Asia–Pacific Microwave Conference.